Chapter 2

Interferometry with coherent light and vortices

This chapter presents an efficient method for generating and detecting optical vortices using pinhole masks. A spiral pinhole array transforms a plane wave into a versatile orbital angular momentum (OAM) spectrum, enabling fine-tuning for single or multiple modes. The setup, based on a Mach-Zehnder interferometer, simplifies amplitude and phase measurements, offering a scalable and practical approach for customizable vortex beam generation. The details theoretical framework and numerical simulation are also discussed in this chapter.

2.1 Introduction

From the past few decades researchers have shown a great deal of interest in optical beams containing orbital angular momentum (OAM), commonly referred to as optical vortices (OVs), because of its special properties [218]. Electromagnetic beams may exhibit OVs during free-space propagation, where the amplitude vanishes and the phase is indeterminate. This characteristic is similar to crystal lattice defects and is known as "screw dislocation" [20]. Such optical beams are characterized by a phase function described as $\exp(il\phi)$, where l is the topological charge (TC), linked to OAM of $l\hbar$ per photon, ħ is the Plank constant in reduced form and ϕ is the azimuthal phase over the transverse plane [19, 219]. The vortex wavevector revolves around the direction of propagation, changing phase by $2\pi l$ in a single cycle to produce a helical wavefront. Unlike spin angular momentum, the OAM has an infinite number of eigenstates that correspond to distinct TCs. This allows it to represent an infinite number of bits and offers an additional degree of freedom. Light beams possessing OAM have led to a growing field of research, resulting in numerous studies and applications. These include particle trapping [92-95], tweezing and manipulation [220], microscopy imaging [100, 101], chiral microstructure fabrication [221], nonlinear optics [222], metrology [107, 108] and several others.

In recent years, a number of techniques have been proposed in response to the growing interests in the generation of the OVs. The conventional methods for producing vortex beams include a SPP with azimuthally varying thickness [24, 25], diffraction by fork grating [37-39], spatial light modulators [31-33], cylindrical lens mode-converters [27-29], q-plates [40, 41], etc. Later, it was proposed that an effective and practical method to generate and detect optical vortices is using a pinhole screen interferometer [44, 224]. Initially, the pinhole screens are distributed symmetrically to determine the TC of Laguerre-Gaussian beams using intensity interference patterns [224]. The technique was then

enhanced by allocating the pinholes at constant radial distance and varying azimuthal angle increments [225]. Thereafter, Li et al. introduced a method based on asymmetrical distribution of pinhole plates to generate and detect higher-order optical vortices [45]. Though majority of these aforementioned techniques can only generate modes with distinct OAM values or direct superpositions of the same. Significantly, beams with a high dimensional and tunable OAM spectrum are beneficial in different applications. In particular, large-capacity optical communications and high-dimensional quantum information processing are made possible by the various OAM states that are available. For optical micro-manipulation, the trapped micro-particles rotation speed is controlled and correlated with the OAM states [226, 227]. Tailoring OAM also find applications in measuring the object parameters [228] and applying geometric operations to images, like rotations and reflections [229]. Later, Yang and colleagues presented a method based on the use of pinhole masks by a spatial light modulator (SLM) for manipulating the OAM spectrum [46]. The spirally arranged distribution of the pinholes helps to tailor the OAM spectrum. The total TC of the vortex is determined by the spiral's shape, which defines the total phase variation among the transmitting fields from different pinholes. They used two different experimental setups to generate and detect the OAM spectra of the vortex beam. In the initial setup, the vortex beam is generated using pinhole masks displayed on the SLM, resulting in the acquisition of only the amplitude component of the generated optical vortex. Whereas, in the second set up they use two SLM's one to generate the vortex beam and second to detect the OAM spectra of the vortex beams.

Here, we present an alternative method to generate and detect the OAM spectra using lithographically fabricated pinhole masks and test accuracy of the generated OAM modes by interferometric and mode projection method. We designed an experimental setup to quantitatively measure amplitude and phase part of the vortex and confirm presence of the

phase singularities in the beam. Also, by projecting the recovered complex field over the helical modes, the compositions of the OAM spectra in the beams are confirmed. By tuning the shape of the spiral pinhole masks, we can tune the OAM spectra. Additionally, with multiple OAM modes we have generated pure OAM modes of the vortex beam. Furthermore, the method is applied to obtain photonic gears in the coherent beam, characterized by the OAM modes with opposite TC superposition, $\pm \boldsymbol{l}$. It was found that photonic gears significantly increase the accuracy of the angle measurement [230] and can be used to measure an object's rotational speed [108].

2.2 Theoretical basis and simulation results

2.2.1 OAM spectrum generation with spiral slit

Bessel beams, particularly zero-order and higher-order ones, are widely recognized for their nondiffracting nature. They propagate with an invariant intensity profile and maintain a constant OAM. The creation of these beams is closely tied to Fourier optics principles. A zero-order Bessel beam can be generated by taking the Fourier transform of an annular aperture. This approach was pioneered by Durnin et al. [231], who demonstrated that placing an annular slit in the back focal plane of a converging lens produces a diffraction pattern with a bright central spot, characteristic of a zero-order Bessel beam as represented in Fig. 2.1 (a). Expanding upon this concept, altering the annular slit to a spiral slit introduces a helical phase structure. Yang and colleagues revealed that wavelets passing through different segments of the spiral slit experience varying optical path lengths [42]. This results in a continuous phase shift across the wavefront, culminating in the emergence of a phase singularity along the beam axis as shown in Fig. 2.1 (b). The structural form of a spiral slit can be mathematically described as

$$r_\theta = \left(r_0^2 + \frac{lz\lambda\theta}{\pi}\right)^{\frac{1}{2}}, \tag{2.1}$$

where r_0 is the initial radius, λ the wavelength, θ is the azimuthal angle, and z is the distance of the spiral slit to the observation plane. This equation defines a Fermat's spiral slit, which produces vortex beams with specific TCs when illuminated by coherent light. Fig. 2.1 shows schematic representation of propagation of a plane wave through annular and spiral slit apertures.

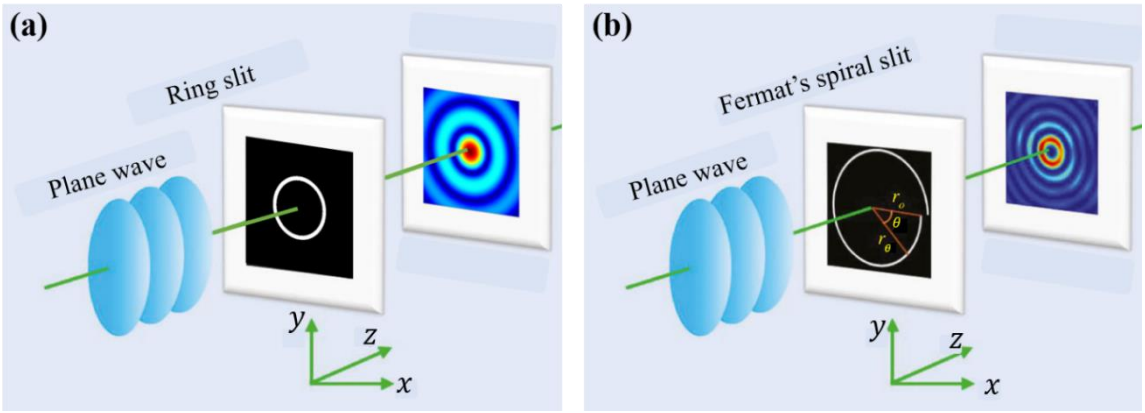

Fig. 2.1 Schematics of propagation of a plane wave through (a) annular aperture (b) spiral slit.

To analyze the beam's behaviour at different propagation planes, Fresnel diffraction is employed. The simulation results depicting the field propagation at an observation plane z, utilizing various types of apertures, are presented in Fig. 2.2. The results demonstrate the transformation of input wavefronts into vortex beams with distinctive helical phase structures, confirming the versatility of spiral slits in generating and controlling structured light. Also, these results provide strong validation for the theoretical predictions, demonstrating a connection between aperture design and the resulting field patterns. The visual comparison confirms the impact of aperture geometry on the diffraction and interference characteristics, thereby reinforcing the theoretical framework with numerical evidence. This alignment underscores the robustness of the model and its potential for broader applications.

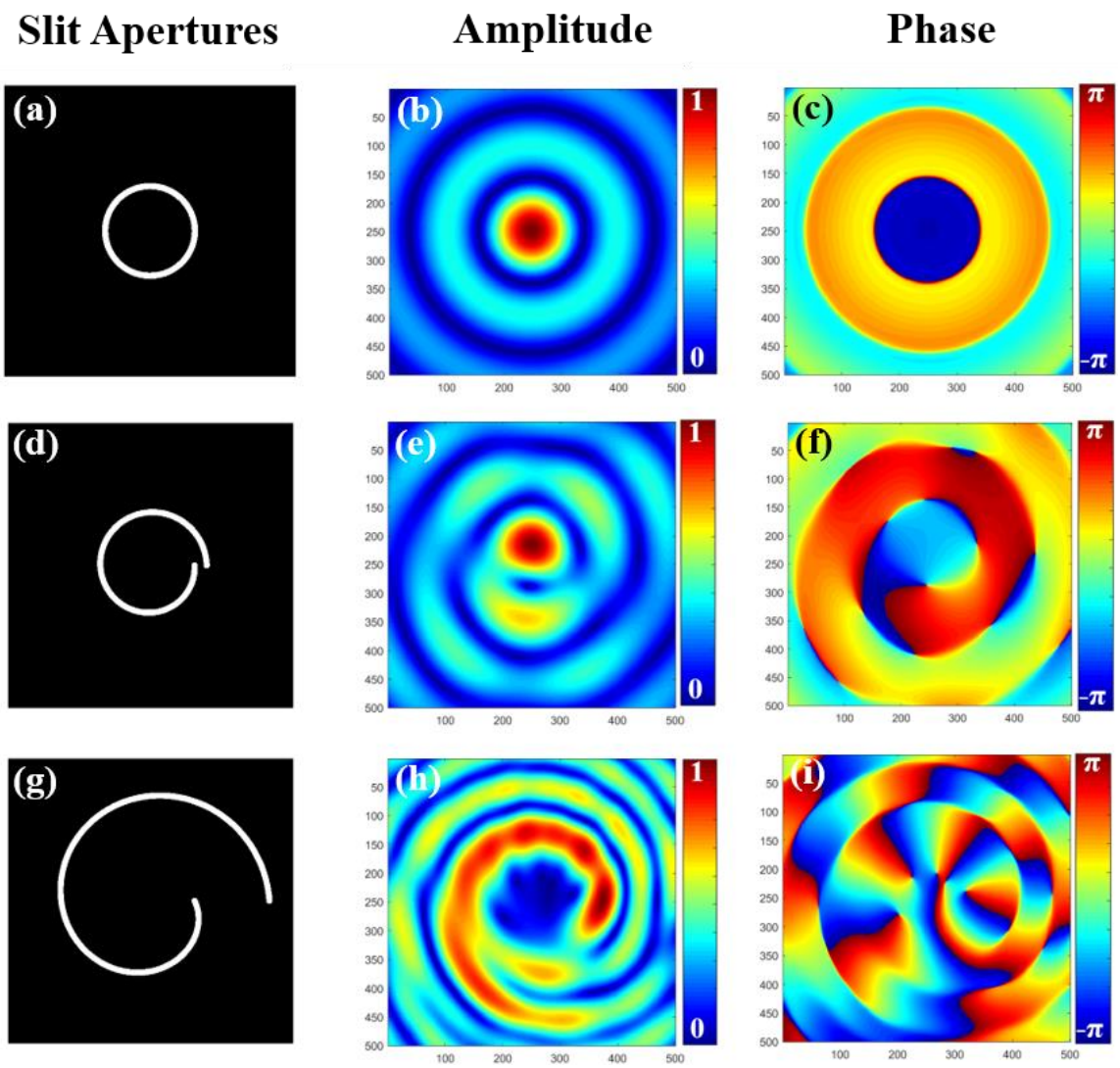

Fig. 2.2 Schematics of the different apertures (a) annular, (d) and (g) spirals with different r_0; (b), (e), and (h) the corresponding simulated amplitude of complex field; (c), (f), and (i) the corresponding simulated phase of complex field.

2.2.2 OAM spectrum generation with pinhole masks

The above formulation pertains to the use of a continuous spiral slit for generating structured beams. However, by discretizing this approach—such as employing pinhole arrays—the method becomes more versatile and generalizable. Discrete pinhole masks enable the creation of intricate beam structures by introducing tailored spatial modulation. This generalized approach allows for the generation of diverse structured beams with enhanced complexity, making it suitable for a variety of applications. Therefore, the binary pinhole masks are made in the form of spiral to introduce a continuous phase shift along

the azimuth to the transmitting wavelets from different pinholes. The azimuthal phase is redistributed by the spiral slit, producing a beam with a spiral phase structure and a wider OAM spectrum centred around a specific value. The pinhole mask $P(\xi,\eta)$ is made up of N number of pinholes, the radius and azimuthal angle of the nth pinhole at transverse (ξ,η) plane is governed by the following relation

$$r(n) = \left(r_0^2 + \frac{lz\lambda\theta(n)}{\pi}\right)^{\frac{1}{2}}, \tag{2.2}$$

and

$$\theta(n) = \frac{2\pi n}{N}, \tag{2.3}$$

where r_0 is the initial radius from the centre to first pinhole, l is the central TC of the vortex, λ is the wavelength of the monochromatic light, and z is the distance from the pinhole mask plane to the observation plane. Fig. 2.3 (a) shows the spiral pinhole mask $P(\xi,\eta)$ at the transverse plane. To generate the vortex beam, we illuminate the pinhole mask with a collimated monochromatic beam and the propagation of the beam from the source is interpreted using the Fresnel diffraction theory [232]. Therefore, the propagated field to a transverse plane (x,y) at a longitudinal distance z is represented as

$$U(x,y,z) = \frac{\exp(ikz)}{i\lambda z}\iint P(\xi,\eta) exp\left\{\frac{ik}{2z}[(x-\xi)^2 + (y-\eta)^2]\right\} d\xi d\eta \tag{2.4}$$

where k is the wave number. The amplitude and phase of the simulated propagated field at a distance $z = 1m$ are shown in Figs. 2.3 (b) and (c), respectively. The parameters for simulation are set as total number of pinholes $N = 50$, wavelength $\lambda = 632.8\,nm$, and initial radius $r_0 = 1mm$.

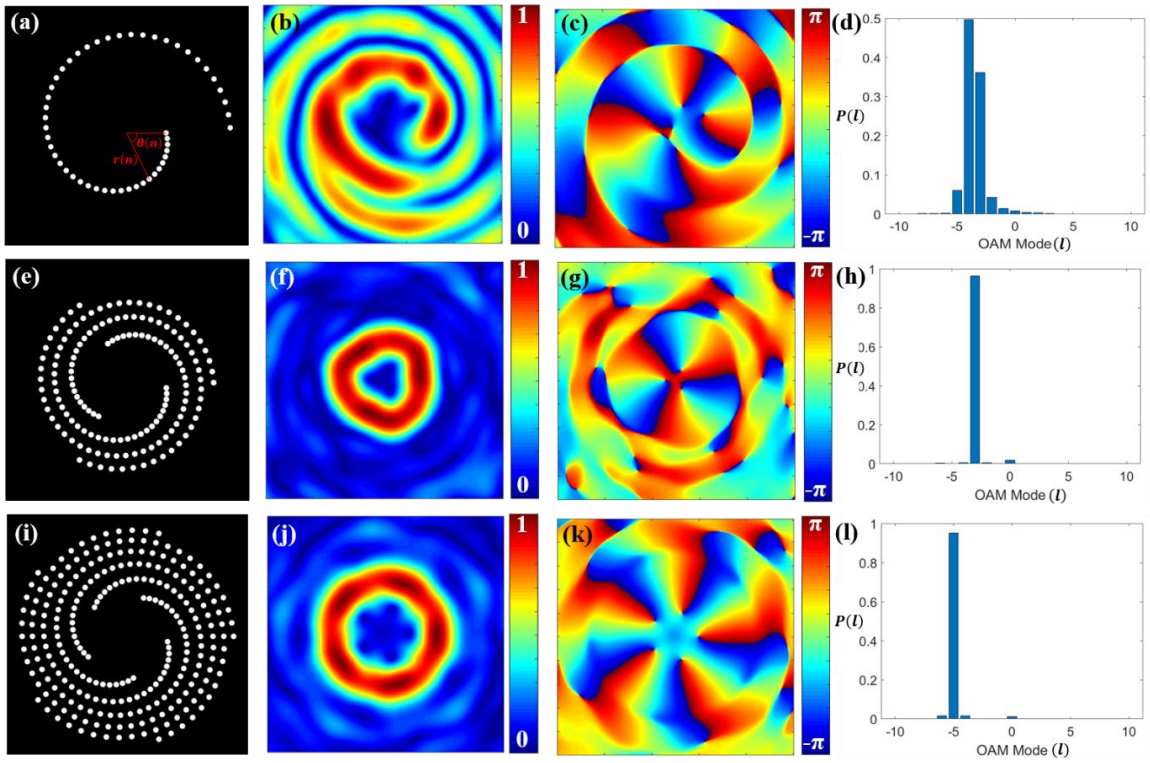

Fig. 2.3 Schematics of the discretized binary spiral pinhole masks (a) single spiral, (e) three spirals, and (i) five spirals; (b), (f), and (j) the corresponding simulated amplitude of complex field; (c), (g), and (k) the corresponding simulated phase of complex field; (d), (h), and (l) the corresponding OAM power spectrum.

To quantitatively examine the OAM spectrum of the coherent beam, we apply the orthogonal projection on the helical basis $\exp(il\phi)$, where l is the TC [233, 234]. To determine the OAM power spectrum, we determine the complex coefficients A_l. Every OAM value has a complex coefficient A_l that varies with the radial coordinates. The complex coefficient A_l is determined by performing an angular Fourier transform on the complex field as follows

$$A_l(r,z) = \frac{1}{2\pi}\int_0^{2\pi} d\phi \exp(-il\phi)\, U(\boldsymbol{r},z), \tag{2.5}$$

where $r \equiv (x,y)$. The OAM power spectrum of the beam is estimated using a numerical integration across the modulus square of A_l with respect to the radial coordinates

$$P(l,z) = \frac{1}{S}\int_0^{\infty} dr\, r|A_l(r)|^2, \tag{2.6}$$

where, $S = \sum \int_0^\infty dr\, r|A_l(r)|^2$ is the beam power and $P(l, z)$ denotes the spectrum at the longitudinal plane z. Thus, the retrieved complex field is substituted in Eqns. (2.5) and (2.6) to retrieve the OAM spectrum of the beam.

Fig. 2.3 (d) represents the retrieved OAM power spectrum using Eqns. (2.5) and (2.6) corresponding to a complex field amplitude and phase of coherent beam as shown in Figs. 2.3 (b) and (c), respectively. Fig. 2.3 (d) shows a wide OAM spectrum of the diffracted complex field from the spiral pinhole mask. Therefore, by adjusting the shape of the spiral slit, the OAM power spectrum can be tailored. The spiral form redistributes the azimuthal phase, leading to a beam with a spiral phase profile and a broader OAM spectrum centred at a specific TC. This straightforward approach enables control over the OAM spectrum by reshaping the beam using a spiral pinhole mask. Additionally, according to the OAM mode selection rule for rotationally symmetric structures, tuning the OAM spectrum to a particular value can be achieved by incorporating multiple identical spirals, evenly spaced along the azimuthal direction. The number of these spirals determines the central TC of the diffracted vortex beam, meaning that if the system features *m*-fold rotational symmetry, the OAM modes will be selected in multiples of *m*. Figs. 2.3 (e) and (i) show examples with three and five spirals, respectively. Figs. 2.3 (f) and (j) illustrate the amplitude, while Figs. 2.3 (g) and 2.3 (k) display the phase distribution of the diffracted field for the corresponding masks. Consequently, beams with specific OAM values of $l = -3$ and $l = -5$ are generated, as indicated by the OAM power spectrum in Figs. 2.3 (h) and 2.3(l).

2.2.3 OAM mode spectrum with $\pm l$ modes

The superposition of OAM modes with opposite TCs $+l$ and $-l$ are termed as photonic gears. To generate a pair of OAM modes, two spiral masks with opposite TC values need to be combined. As a result, the radial and azimuthal positions of the nth pinhole in the mth spiral can be described by the following equations

$$\mathrm{r}(n,m) = \pm\left(r_0^2 + \frac{lz\lambda\theta(n,m)}{\pi}\right)^{\frac{1}{2}}, \tag{2.7}$$

and

$$\theta(n,m) = \pm\left(\frac{2\pi n}{N} + \frac{2\pi m}{M}\right), \tag{2.8}$$

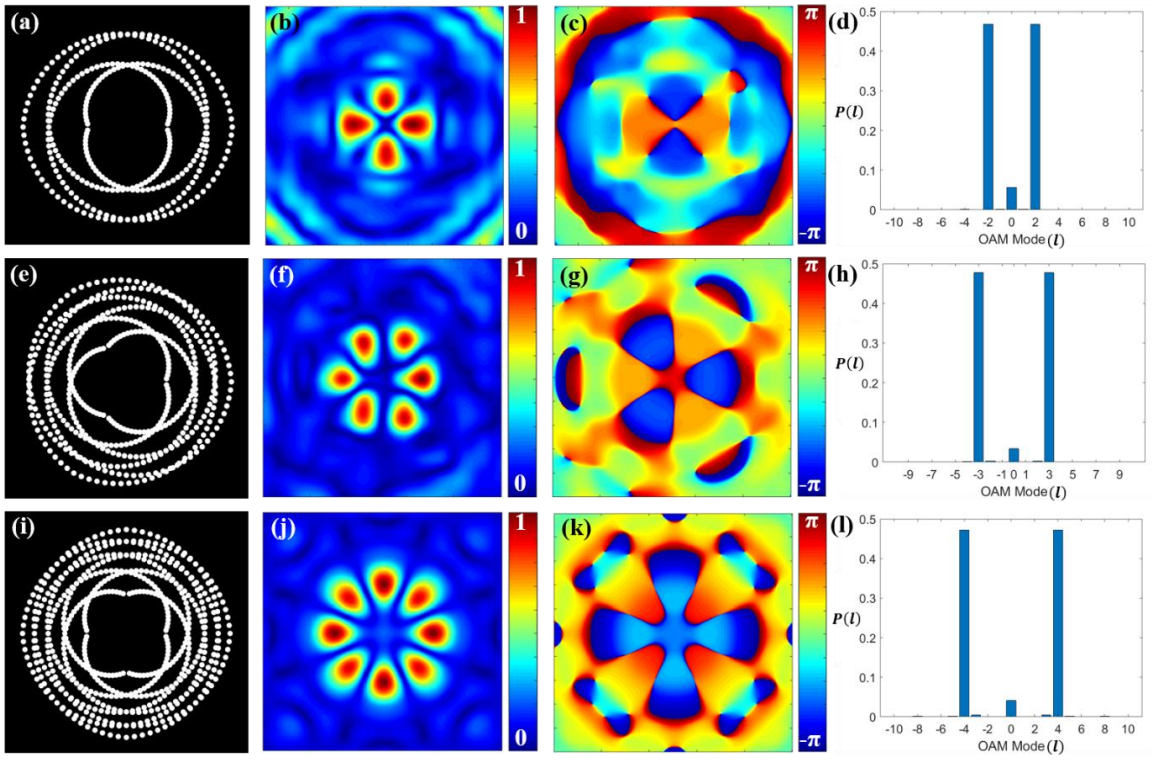

Fig. 2.4 Schematics of the pinhole gears (a) $\boldsymbol{l = \pm 2}$, (e) $\boldsymbol{l = \pm 3}$, and (i) $\boldsymbol{l = \pm 4}$; (b), (f), and (j) the corresponding simulated amplitude of complex field; (c), (g), and (k) the corresponding simulated phase of complex field; (d), (h), and (l) the corresponding OAM power spectrum.

The binary masks designed to create the superposition of coherent modes $l = \pm 2$, $l = \pm 3$, and $l = \pm 4$ are illustrated in Figs. 2.4 (a), (e), and (i), respectively. It is widely recognized that the superposition of two vortex beams with opposite TCs results in an intensity pattern consisting of $2l$ petal-like structures. This phenomenon is clearly illustrated by the simulated amplitude patterns of the diffracted wave shown in Figs. 2.4 (b), (f), and (j). The associated phase distributions are depicted in Figs. 2.4 (c), (g), and (k), while the corresponding OAM spectra are presented in Figs. 2.4 (d), (h), and (l).

2.3 Experiment

An interferometric system as shown in Fig. 2.5 is setup to verify generation of the OAM modes and vortices in the coherent beam. A He-Ne laser with a wavelength of 632 nm [Thorlabs, HNL150L] is filtered through a spatial filter and collimated using a bi-convex lens with a focal length of 10 cm. The collimated beam splits by a beam splitter BS1 into two arms of equal intensity: one arm contains the binary pinhole mask, while the other serves as a reference for the interferometric measurement. A binary pinhole mask is fabricated using lithography technique followed by wet etching method. A 100 nm chrome coated glass plate was used as a substrate and a positive photoresist (S1813 from Micro Resist Technology, Germany) was spin coated on it. To print the mask on the substrate and construct the appropriate structures, Intelligent Micropatterning USA's SF-100 maskless lithography equipment was used. After development, the substrate was submerged in chrome etchant (Etch-18, from Micro Resist Technology, Germany) to remove chrome from exposed areas. Eventually, the photoresist was removed and the substrate was cleaned in order to obtain the necessary mask structures.

The light diffracted from the pinhole mask interferes with the reference beam from the other arm at beam splitter BS2. A neutral density filter is placed in the reference arm to adjust the intensity and enhance the interference fringe visibility. A carrier frequency is introduced in the reference beam with a mirror M1, and the interference pattern is recorded by a charged-couple device (CCD).

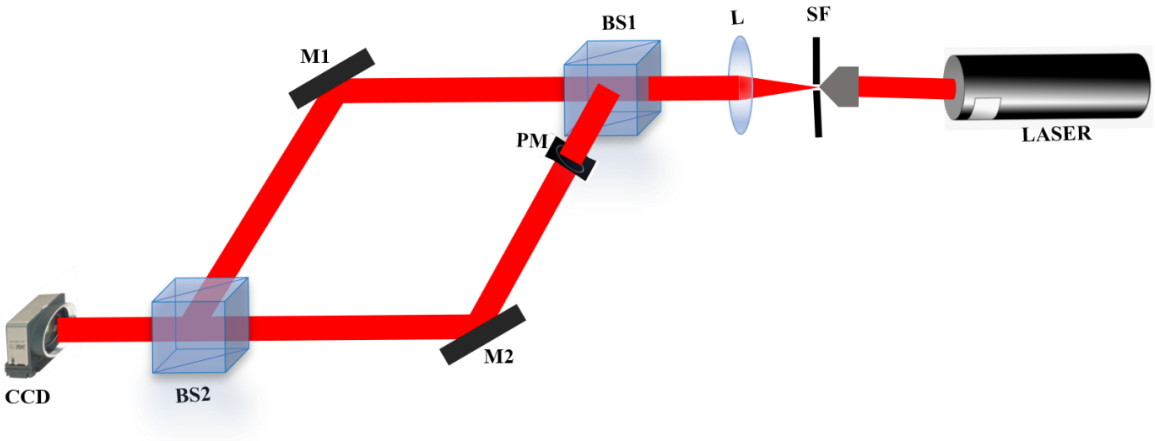

Fig. 2.5 Experimental setup: SF: Spatial Filter, L: Lens, BS: Beam Splitter, PM: Binary Pinhole Mask, M: Mirror, CCD: Charge-Coupled Device.

2.4 Results and discussion

A vortex beam, emerging from the pinhole mask PM, at the CCD plane is represented as

$$U_P(x,y) = |A(x,y)|\exp\left[i\phi(x,y)\right] \tag{2.9}$$

where $|A(x,y)|$ is the amplitude and $\phi(x,y)$ is the phase of the complex field.

A reference field at the CCD plane is represented as

$$U_R(x,y) = \exp\left[-i2\pi\left(f_{x0}x + f_{y0}y\right)\right] \tag{2.10}$$

where $\left(f_{x0}, f_{y0}\right)$, is the spatial carrier frequency of the reference field.

Therefore, the interference pattern at the CCD plane is

$$I(x,y) = 1 + |A(x,y)|^2 + |A(x,y)|\exp[i\phi(x,y)]\exp\left[i2\pi\left(f_{x0}x + f_{y0}y\right)\right] +$$

$$|A(x,y)|\exp[-i\phi(x,y)]\exp\left[-i2\pi\left(f_{x0}x + f_{y0}y\right)\right] \tag{2.11}$$

$$I(x,y) = I_0(x,y) + |A(x,y)|\exp[i\phi(x,y)]\exp\left[i2\pi\left(f_{x0}x + f_{y0}y\right)\right] +$$

$$|A(x,y)|\exp[-i\phi(x,y)]\exp\left[-i2\pi\left(f_{x0}x + f_{y0}y\right)\right] \tag{2.12}$$

where $I_0(x,y) = 1 + |A(x,y)|^2$ is an unmodulating DC term.

We retrieve the complex field of the vortex beam by the Fourier fringe analysis of the interferogram, and the Fourier spectrum of the interference pattern is represented as [235]

$$G\left(f_x, f_y\right) = A\left(f_x, f_y\right) + C\left(f_x - f_{x0}, f_y - f_{y0}\right) + C^*\left[\left(f_x + f_{x0}\right), \left(f_y + f_{y0}\right)\right] \tag{2.13}$$

where $G(f_x, f_y) = \text{FT}[I(x,y)]$, FT represents two-dimensional Fourier transform. Similarly, $A(f_x, f_y) = \text{FT}[I_0(x,y)]$, and the second and third terms on the right side of Eq. (2.13) correspond to the Fourier transforms of the second and third terms in Eq. (2.12), respectively. This enables one to obtain $C(f_x,\ f_y)$, the Fourier spectrum of the complex amplitude given by $c(x,y) = |A(x,y)|\exp[i\phi(x,y)]$. By selectively filtering the second spectral component $C(f_x - f_{x0}, f_y - f_{y0})$ associated with the carrier frequency (f_{x0}, f_{y0}) and shifting it to the origin, the carrier frequency can be effectively eliminated. Therefore, the reference field $U_R(x,y) = \exp\left[-i2\pi(f_{x0}x + f_{y0}y)\right]$ introduces a known spatial carrier frequency (f_{x0}, f_{y0}). This shifts the vortex beam's spectrum $C(f_x,\ f_y)$ (Eq. 2.13) away from the origin in Fourier space, separating it from the DC term $A(f_x, f_y)$ (centered at zero frequency) and the conjugate term C^*(shifted to $(-f_{x0}, -f_{y0})$). This separation guarantees that the three components in Eq. (2.13) do not overlap in the Fourier domain, provided the carrier frequency is chosen to be sufficiently large (Nyquist criterion) [235]. Thus, the spatial carrier frequency ensures $C(f_x,\ f_y)$ is isolated without aliasing or overlap, preserving the one-to-one mapping between the filtered spectrum and the retrieved field ensuring the uniqueness of the inverse Fourier transform.

The principle of Fourier fringe analysis is shown in Fig. 2.6. Fig. 2.6 (a) shows a recorded interferogram at the CCD plane. Fig. 2.6 (b) shows the Fourier spectra represented by Eq. (2.13). The vortex beam spectrum is shifted by (f_{x0}, f_{y0}) from the origin in the Fourier space due to the spatial carrier frequency, while its conjugate is shifted in the other direction. One of the spectra is filtered and brought back to the centre as shown in Fig. 2.6 (c). Inverse Fourier transform of the filtered spectrum retrieves the complex field of the vortex beam as shown in Fig. 2.6 (d) and (e), respectively.

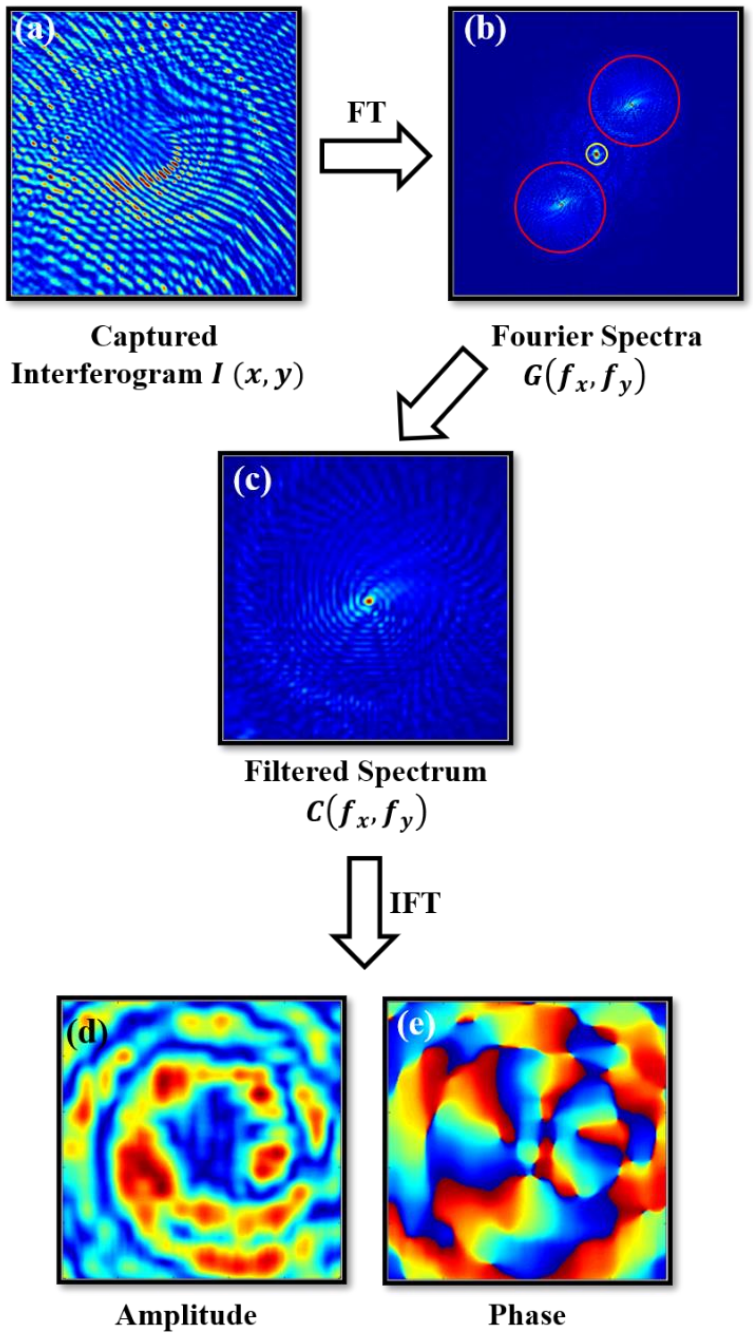

Fig. 2.6 Pipeline for the Fourier fringe analysis, where FT denotes Fourier Transform and IFT denotes Inverse Fourier Transform.

Fig. 2.7 shows experimental results corresponding to the simulation results as shown in Fig. 2.3. The binary spiral pinhole masks with one spiral, three spirals, and five spirals, respectively, are shown in Figs. 2.7 (a), (e), and (i). The experimental results for the corresponding complex field distribution are retrieved from the interference fringes using the Fourier fringe analysis. The amplitude distributions of the coherent complex fields are

shown in Figs. 2.7 (b), (f), and (j), and the corresponding phase distributions are shown in Figs. 2.7 (c), (g), and (k). The related OAM mode spectrum, which shows the power weight distribution of helical modes, is shown in Figs. 2.7 (d), (h), and (l). As a result, there is a good agreement between the modelling findings Fig. 2.3, and the experimental results Fig. 2.7. The transmission efficiency of the lithographically fabricated binary pinhole masks is a critical factor in the generation of complex fields. The binary pinhole masks, while reducing transmission efficiency due to their opaque regions, were designed to prioritize precise spatial mode control. Larger pinholes would increase efficiency but degrade OAM selectivity, while smaller pinholes would exacerbate losses. Therefore, the pinhole diameter (150 μm) and distribution were optimized to balance mode purity and transmission. Losses were mitigated by using a high-brightness source.

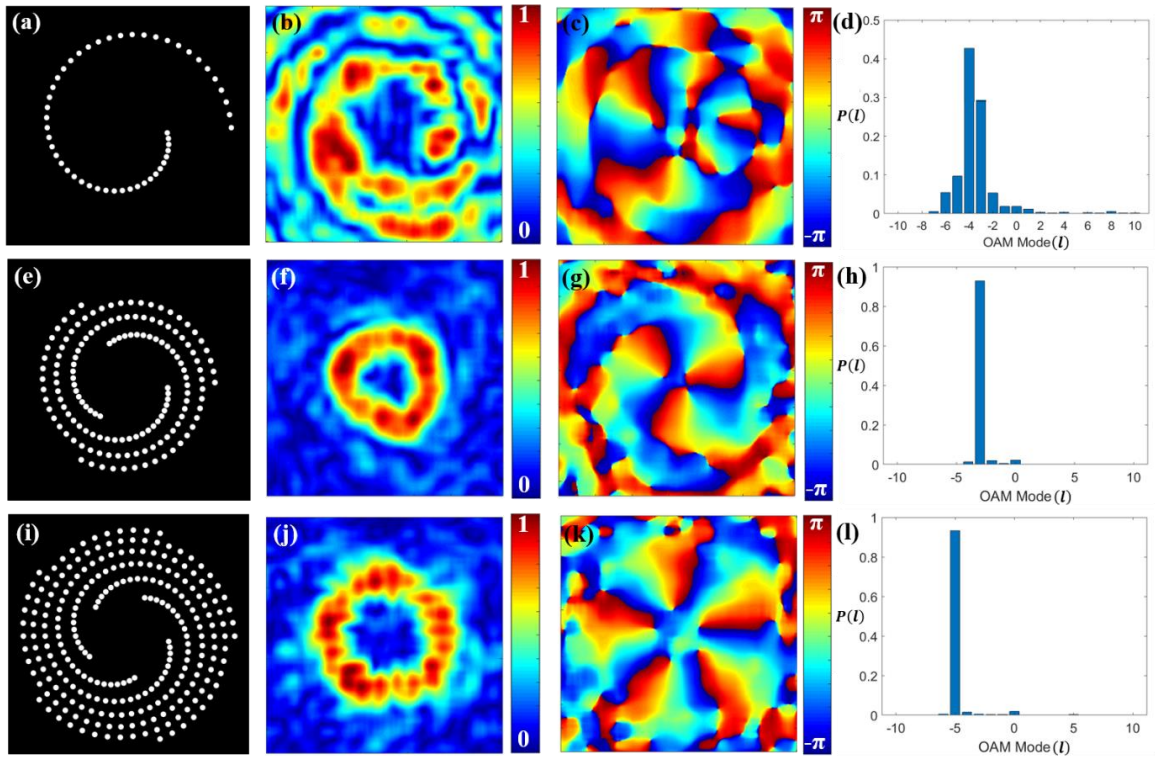

Fig. 2.7 Experimental results. (a) single spiral, (e) three spirals, and (i) five spirals; (b), (f), and (j) the corresponding simulated amplitude of complex field; (c), (g), and (k) the corresponding simulated phase of complex field; (d), (h), and (l) the corresponding OAM power spectrum.

Fig. 2.8 shows our experimental results, corresponding to the simulations results, shown in Fig. 2.4 for pinhole gears. The binary pinhole masks with superposition of modes $l = \pm 2$, $l = \pm 3$, and $l = \pm 4$ are displayed in Figs. 2.8 (a), (e), and (i), respectively. The experimental results for the corresponding amplitude distribution of the complex field are shown in Figs. 2.8 (b), (f), and (j), and the corresponding phase distribution are shown in Figs. 2.8 (c), (g), and (k). The related OAM mode spectrum, which shows the power spectrum of helical modes, is shown in Figs. 2.8 (d), (h), and (l). The comparison between simulation results Fig. 2.4 and experimental results Fig. 2.8 shows that the models and experimental findings agree well, indicating the usefulness of structured pinhole masks for the production of photonic gears.

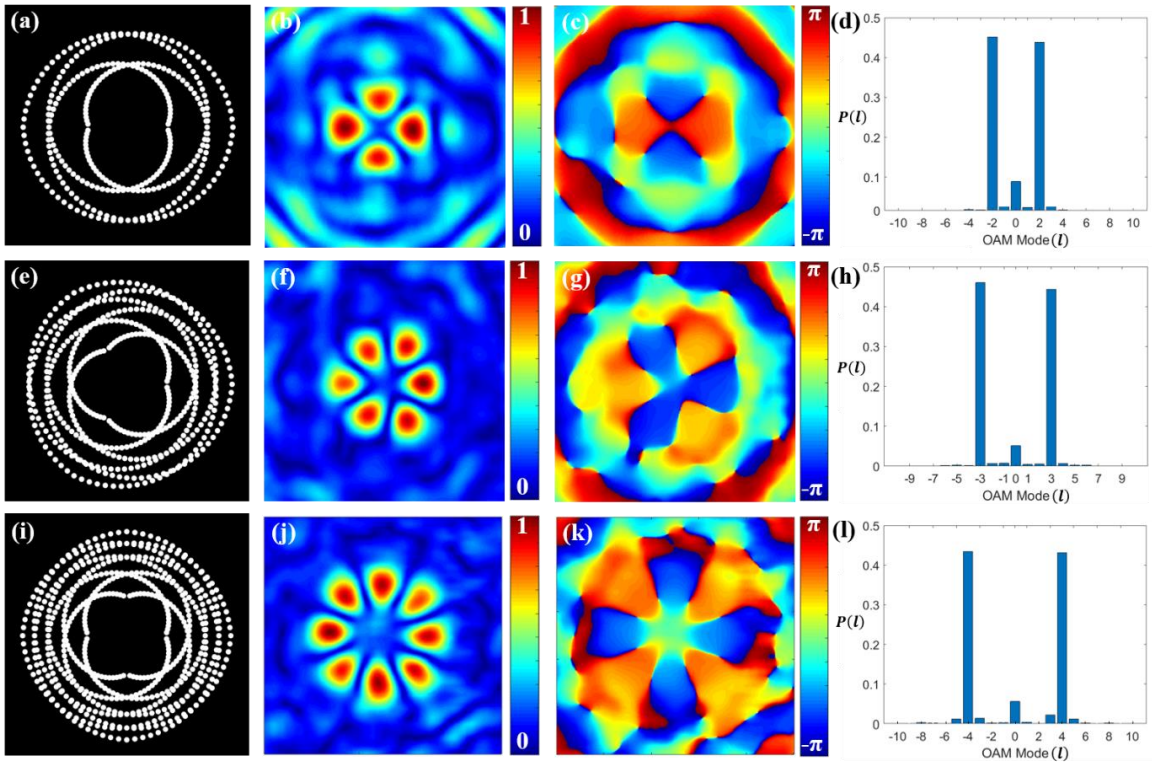

Fig. 2.8 Experimental results. Schematics of the pinhole gears (a) $\boldsymbol{l = \pm 2}$, (e) $\boldsymbol{l = \pm 3}$, and (i) $\boldsymbol{l = \pm 4}$; (b), (f), and (j) the corresponding simulated amplitude of complex field; (c), (g), and (k) the corresponding simulated phase of complex field; (d), (h), and (l) the corresponding OAM power spectrum.

2.5 Conclusion

In this work, we developed a simple technique to generate and detect the optical vortices using lithographically fabricated binary pinhole masks. With fixed TC, the technique also used for tailoring the multiple OAM spectrum and to produce the superposition of OAM modes with opposite TC. Presence of vortices and OAM spectra in the beam is experimentally tested and confirmed by the interferometric method and projection of the coherent complex field over the helical basis. Owing to its distinct configuration, this kind of pinhole mask can be further investigated for matter waves, such as in the context of photon sieves and Vogel spiral array.